

No-Arbitrage Deep Calibration for Volatility Smile and Skewness

Kentaro Hoshisashi, Carolyn E. Phelan, Paolo Barucca

k.hoshisashi@ucl.ac.uk

Department of Computer Science
University College London
London, United Kingdom

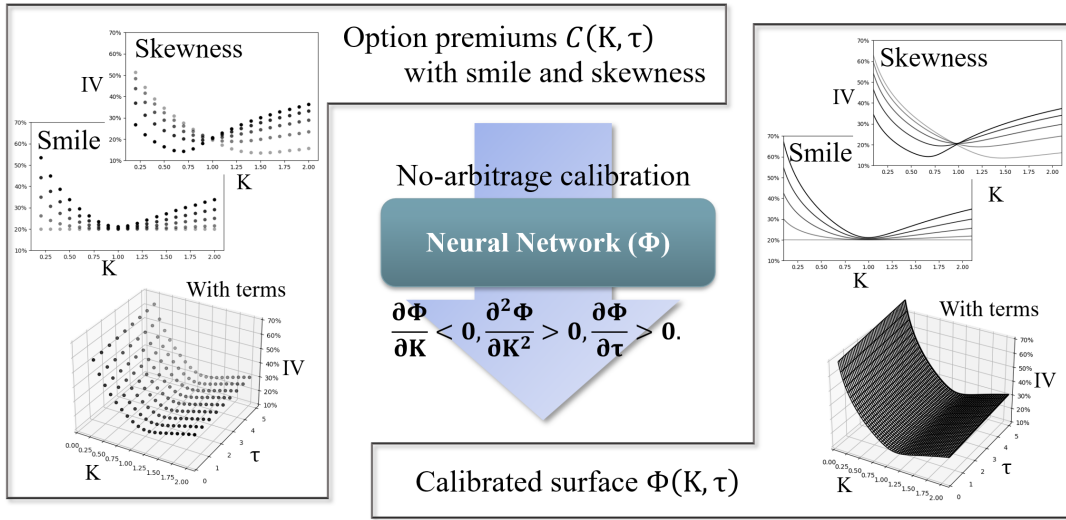


Figure 1: The conceptual scheme of no-arbitrage deep calibration for volatility smile and skewness

ABSTRACT

Volatility smile and skewness are two key properties of option prices that are represented by the implied volatility (IV) surface. However, IV surface calibration through nonlinear interpolation is a complex problem due to several factors, including limited input data, low liquidity, and noise. Additionally, the calibrated surface must obey the fundamental financial principle of the absence of arbitrage, which can be modeled by various differential inequalities over the partial derivatives of the option price with respect to the expiration time and the strike price. To address these challenges, we have introduced a Derivative-Constrained Neural Network (DCNN), which is an enhancement of a multilayer perceptron (MLP) that incorporates derivatives in the output function. DCNN allows us to generate a smooth surface and incorporate the no-arbitrage condition thanks to the derivative terms in the loss function. In numerical experiments, we apply the stochastic volatility model with smile and skewness parameters and simulate it with different settings to examine the stability of the calibrated model under different conditions. The results show that DCNNs improve the interpolation of the implied volatility surface with smile and skewness by integrating the computation of the derivatives, which are necessary and sufficient no-arbitrage conditions. The developed algorithm also offers practitioners an effective tool for understanding expected market dynamics and managing risk associated with volatility smile and skewness.

CCS CONCEPTS

- Computer systems organization → Neural networks;
- Computing methodologies → Neural networks;
- Mathematics of computing → Multivariate statistics;
- Information systems → Expert systems;
- Theory of computation → Nonconvex optimization;
- Fixed parameter tractability;
- Applied computing → Economics;
- Networks → Network performance analysis.

KEYWORDS

volatility surface, neural networks, deep learning, no-arbitrage constraints, gradient-based learning, partial differential equations, Derivative-Constrained Neural Network

1 INTRODUCTION

Implied volatility (IV) is the volatility that is hypothesized to make sense of empirical option prices, i.e. implied volatility is the value of volatility which would result in the market price using the Black-Scholes formula.

The standard calibration of the premium surface requires us to find a solution to the Black-Scholes partial differential equation (PDE). Traditional calibration involves minimizing the difference between values predicted by a model and those observed. In finance, the no-arbitrage conditions ensure that the price of the derivative is fixed at the same level as the value of the replicating portfolio [16]. Under these conditions, it is a necessary and sufficient condition that certain derivatives of the option prices should satisfy certain

derivative inequalities [10]. Taking into account the no-arbitrage conditions enhances the robustness and interpretability of the calibration of the premium surface. In financial applications, this is particularly beneficial for interpolating option premiums in the face of sparse market data while adhering to no-arbitrage conditions.

In such a situation, researchers have been investigating how effective the artificial neural networks (ANNs) approach is applied to the calibration problem in the options market, based on its use as a universal approximator [15, 24, 25]. In this study, we expand the standard ANNs backpropagation with derivative terms in the loss function, incorporated into the calibration process, enhancing accuracy. Specifically, this study proposes a Derivative-Constrained Neural Network (DCNN), which is the expansion of a multilayer perceptron (MLP) with Automatic Differentiation (AD) to compute the exact derivatives simultaneously. This approach ensures the network's differentiability, which is essential for representing derivative functions of the original function of MLP, with an expansion of an MLP with reverse AD that generates the first and second derivatives efficiently [47]. The resulting network has a deep learning architecture that allows the efficient computation of the derivatives and can therefore introduce differential soft constraints for the generated surface.

To evaluate the representation capability of smile and skewness features in IV surfaces [14, 44], we use one of the stochastic volatility models, the Stochastic Alpha Beta Rho (SABR) model [22], often used by practitioners. We utilize sparse option premiums generated using the SABR model and evaluate the ability to reproduce premiums and risk profiles which retain the characteristics of volatility smile and skewness. Through our DCNN network, the interpolation of the premium surface is improved, benefiting from the efficient computation of derivatives and the consideration of no-arbitrage conditions. We also demonstrate that this model serves as a powerful tool for practitioners to understand the expected market dynamics and manage risks with volatility smile and skewness.

2 BACKGROUND AND LITERATURE REVIEW

The effectiveness of ANNs in addressing function approximation problems has been thoroughly researched across several fields. The fields that bear relevance to this study are detailed below.

2.1 Volatility smile and skewness

In the early 1970s, the Black-Scholes model [7] facilitated the pricing of options based on the assumption that the underlying asset's volatility is constant. However, empirical observations revealed that options with different strike prices actually implied varied volatilities, known as the volatility smile and skewness [14, 44]. Numerous local volatility models [17, 18] attempted to account for the reproduction of the static pattern of the smiles. Effective prediction of their dynamics was made possible by the introduction of stochastic volatility models [22, 23, 28]. One common practical approach is the SABR stochastic volatility model [22], which employs parameters to characterize the smile and skewness in its stochastic differential equations. However, the dynamics of the volatility smile are still not perfectly represented, necessitating frequent recalibration to align the model with market data. Related to these challenges, the potential of ANNs for solving PDEs has been explored in [3, 11, 32].

2.2 Financial applications of ANNs

Previous research into finding option premiums using ANNs has primarily focused on IV and has often employed adapted global optimization methods [12, 13, 35]. Additionally, there have been applications of advanced network models, such as variational autoencoders [5], generative Bayesian models [30], hybrid gated NN [9], and Vol GANs [13]. Several studies have addressed the calibration problems of option products by penalizing the loss using soft constraints [1, 12, 13, 29] or mapping pricing from model parameters [4, 26, 38]. A comprehensive review of ANNs methods for option pricing was conducted in [45].

2.3 Multi-task deep learning

Multi-task deep learning [48, 54] and multi-objective optimization [21] address the challenge of weighing multiple loss functions to obtain better performance [31, 37] with both soft and/or hard constraints for ANNs. In this context, the introduction of derivative terms in the loss function to fit full PDEs has been explored in physics-informed neural networks (PINNs) [41], and in DCNNs [36] where isolated derivative terms are considered [40, 52, 53].

3 CALIBRATION PROBLEM

The calibration of volatility surfaces or option prices is an important inverse problem in quantitative finance. In [18], the author has proposed the local volatility model, in which the European options prices satisfy the PDE of the following form with the current price of an underlying asset $S_t > 0$,

$$C - \frac{1}{2}\sigma^2(K, \tau)K^2 \frac{\partial^2 C}{\partial K^2} + \frac{\partial C}{\partial \tau} + rK \frac{\partial C}{\partial K} = 0, \quad (1)$$

with initial and boundary conditions given by

$$C(K, 0) = (S_T - K)^+, \quad \lim_{K \rightarrow \infty} C(K, \tau) = 0, \quad \lim_{K \rightarrow 0} C(K, \tau) = S_0, \quad (2)$$

where K is the strike price and τ is the option term to expiry T from valuation date t , and $C = C(K, \tau)$ is the value of the European call option with expiration date T , strike price K with $K, \tau \in [0, \infty)$, and a risk-free rate r . The inverse problem of the implied volatility model is that, given limited options prices, we would like to know the premium function $C(K, \tau)$ or an implied volatility surface $\sigma(K, \tau)$, which gives these options prices via the Black-Scholes formula. The challenge of this inverse problem is the scarcity of options price data. To solve this, possibilities are to interpolate/extrapolate the price data or add further information that helps solve a problem.

3.1 No-arbitrage constraints of European options

The calibration of option prices is limited by sparse data and, as discussed, should obey the constraints imposed by the no-arbitrage conditions. The no-arbitrage principle posits that market prices prevent guaranteed returns above the risk-free rate, and any equivalent asset must have the same price across markets. We consider the necessary and sufficient conditions for no-arbitrage, reported in [10] and implemented in [2, 19, 43], as the constraints that our surface needs to satisfy. This allows us to appropriately express the call option price as a two-dimensional surface. The necessary and

sufficient conditions for no-arbitrage are represented as inequalities for the first and second derivatives,

$$-e^{-r\tau} \leq \frac{\partial C}{\partial K} \leq 0, \quad \frac{\partial^2 C}{\partial K^2} \geq 0, \quad \frac{\partial C}{\partial \tau} \geq 0. \quad (3)$$

In Eq. (3), no-arbitrage conditions require these derivatives to have a specific sign. The standard architecture does not automatically satisfy these conditions when calibrating with a loss function simply based on the mean squared error (MSE) for the prices.

3.2 ANNs with No-arbitrage Constraints

Here, we can consider the problem as a calibration problem of an approximated function defined by the ANNs, $\Phi(K, \tau)$. Having described each derivative constraint using the function Φ , we can now introduce the total cost function with no-arbitrage constraints for European (call) options to minimise,

$$E(C, \Phi_{W,b}) = E_{\text{MSE}} + E_{\mathcal{P}}, \quad (4)$$

$$E_{\text{MSE}} = \frac{1}{N} \sum_{i=1}^N \{C(K_i, \tau_i) - \Phi(K_i, \tau_i)\}^2. \quad (5)$$

Here, $C(K_i, \tau_i)$ is the observed premium for the indexed values of strike K_i and time to expiry τ_i , $i = 1, \dots, N$ from the observed dataset. The penalty term $E_{\mathcal{P}}$ represents a score of the total no-arbitrage conditions involving the first and second derivatives,

$$E_{\mathcal{P}} = \frac{1}{M} \sum_{j=1}^M \left\{ \lambda_{m_1} \left(h_K \frac{\partial \Phi(\hat{K}_j, \hat{\tau}_j)}{\partial \hat{K}_j} \right) + \lambda_{m_2} \left(h_{KK} \frac{\partial^2 \Phi(\hat{K}_j, \hat{\tau}_j)}{\partial \hat{K}_j^2} \right) + \lambda_{m_3} \left(h_{\tau} \frac{\partial \Phi(\hat{K}_j, \hat{\tau}_j)}{\partial \hat{\tau}_j} \right) \right\}. \quad (6)$$

The set of \hat{K} and $\hat{\tau}$ values in which we evaluate the derivatives can be obtained with a mesh grid, $j = 1, \dots, M$. The h terms are sign-adjustment coefficients, which make sure that the signs of the penalty terms are correct, $h_K = (1, 0)$, $h_{KK} = (-1, 0)$, $h_{\tau} = (0, -1)$. $\lambda_m(x)$ is an intensifier of derivative losses in the total cost,

$$\lambda_m(x) = \begin{cases} m \cdot g(x), & \text{if penalty} \\ 0, & \text{if not penalty} \end{cases} \quad (7)$$

where $m \in \mathbb{R}$ are constants and $g(x)$ are intensifier functions, which can be non-linear.

4 DERIVATIVE-CONSTRAINED NEURAL NETWORK (DCNN)

This section introduces the Derivative-Constrained Neural Network (DCNN) as an expansion of the work in [36], which efficiently computes the partial derivatives of a neural network function with respect to its input features. We consider a simple feed-forward neural network architecture, a multilayer perceptron (MLP). Let $L \geq 2$ be an integer representing the depth of the network; we consider a neural network constructed with one input vector, L hidden layers, and one output value. Both the input values and the output variable are real numbers, i.e., $\mathbf{x} \in \mathbb{R}^n$ and $y \in \mathbb{R}$. We can consider the MLP as a multivariate function Φ depending on the variables \mathbf{x} , i.e. $\Phi : \mathbf{x} \mapsto y$,

$$y = \Phi(\mathbf{x}) = A_L \circ f_{L-1} \circ A_{L-1} \circ \dots \circ f_1 \circ A_1(\mathbf{x}), \quad (8)$$

where for $l = 1, \dots, L$, $A_l : \mathbb{R}^{d_{l-1}} \rightarrow \mathbb{R}^{d_l}$ are affine functions as $A_l(\mathbf{x}_{l-1}) = W_l^T \mathbf{x}_{l-1} + \mathbf{b}_l$, and d_l is the number of neurons in the next layer l for $\mathbf{x}_{l-1} \in \mathbb{R}^{d_{l-1}}$, with $W_l \in \mathbb{R}^{d_{l-1} \times d_l}$ and $\mathbf{b}_l \in \mathbb{R}^{d_l}$, $d_0 = n$, $d_L = 1$, and $\mathbf{x}_0 = \mathbf{x}$. f_l is an activation function which is applied component-wise. Given a dataset \mathbf{X} , which includes a set of pairs $(\mathbf{x}^{(i)}, y^{(i)})$, $i = 1, \dots, N$, and a cost function $E(\mathbf{X}, \Phi_{W,b})$, the network model Φ is found by fitting the values of W and \mathbf{b} which minimize the cost function.

We consider optimization problems which include losses, not only associated with the network function $\Phi(\mathbf{x})$, but also its derivatives. The total cost includes several terms, which account for the derivatives,

$$E(\mathbf{X}, \hat{\mathbf{X}}, \Phi_{W,b}) := \frac{1}{N} \sum_{i=1}^N \left(y^{(i)} - \Phi_{W,b}(\mathbf{x}^{(i)}) \right)^2 + \frac{1}{M} \sum_{j=1}^M \left\{ \lambda_{m_1}(\nabla \Phi_{W,b}(\hat{\mathbf{x}}^{(j)})) + \lambda_{m_2}(\nabla^2 \Phi_{W,b}(\hat{\mathbf{x}}^{(j)})) \right\}, \quad (9)$$

where, $\hat{\mathbf{x}}$ is input features and $\hat{\mathbf{x}}^{(j)}$ for derivative losses in computational grids $\hat{\mathbf{X}}$. ∇ and ∇^2 are partial derivative vectors respectively,

$$\nabla \Phi(\mathbf{x}) = \left[\frac{\partial \Phi}{\partial x_1}, \frac{\partial \Phi}{\partial x_2}, \dots, \frac{\partial \Phi}{\partial x_n} \right]^T, \quad \nabla^2 \Phi(\mathbf{x}) = \left[\frac{\partial^2 \Phi}{\partial x_1^2}, \frac{\partial^2 \Phi}{\partial x_2^2}, \dots, \frac{\partial^2 \Phi}{\partial x_n^2} \right]^T, \quad (10)$$

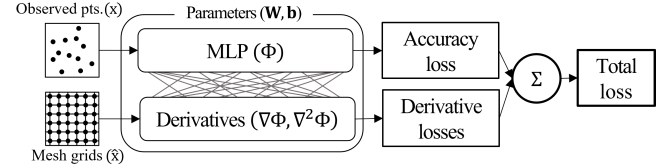


Figure 2: The whole network architecture of Derivative-Constrained Neural Network (DCNN). It is an expansion of a multilayer perceptron (MLP) with additional networks that simultaneously generate its first and second derivatives.

Using Eq. (9) as the cost function, the optimizer uses gradients with respect to the parameters (i.e., W , \mathbf{b}) for updates. A challenge lies in that Eq. (9) involves derivatives with respect to \mathbf{x} , also functions of the parameters. When numerical approximation of derivatives is used, it could result in slow or inaccurate solutions. To solve this, this study utilizes DCNN, an extended backpropagation algorithm [46] with Automatic Differentiation, for the gradient in Eq. (9) through exact derivative formulations. Following [53] and [40], the first derivatives of a layer in Φ is

$$\nabla_l := \frac{\partial \mathbf{x}_l}{\partial \mathbf{x}} = \{f'_l \circ A_l(\mathbf{x}_{l-1}) * W_l^T\} \nabla_{l-1}, \quad (11)$$

with $*$ denoting tensor broadcasting [49]. We then compute the first derivative of Φ , i.e., $\nabla \Phi$, by sequentially applying the chain rule in Eq. (11). Note, f'_l of the last layer and ∇_{l-1} of the first layer aren't applied in Eq. (11). For the second derivative of Φ , we use the definition $\partial^2 \Phi / \partial x^2 = \partial(\partial \Phi / \partial x) / \partial x$. The second derivative of

each layer is described as

$$\begin{aligned}\nabla_l^2 &:= \frac{\partial^2 \mathbf{x}_l}{\partial \mathbf{x}^2} = f_l'' \circ A_l(\mathbf{x}_{l-1}) * \{W_l^\top \nabla_{l-1}\}^{\circ 2} \\ &\quad + \{f_l' \circ A_l(\mathbf{x}_{l-1}) * W_l^\top\} \nabla_{l-1}^2.\end{aligned}\quad (12)$$

and $\{\cdot\}^{\circ 2}$ is the operation of the Hadamard product for element-wise [42]. Subsequently, $\nabla^2 \Phi(\mathbf{x})$ is obtained using Eqs. (11) and (12) with the chain rule. These formulations require MLP activation functions to be second-order differentiable or higher. It is noted that functions like Relu or Elu need slight additional consideration at non-differentiable singular points. If all activation functions are second-order differentiable, the same is true for the whole network [25].

4.1 Algorithms

The Derivative-Constrained Neural Network (DCNN) algorithm efficiently computes the partial derivatives of a neural network function with respect to its input features.

Algorithm 1 Derivative-Constrained Neural Network Algorithm

Require: Training dataset of size $N \mathbf{X} : (\mathbf{x}^{(i)}, y^{(i)}), i = 1, \dots, N$
1: Mesh grid points of size $M \hat{\mathbf{X}} : \hat{\mathbf{x}}^{(j)}, j = 1, \dots, M$
2: An MLP Φ with L layers, $l = 1, \dots, L$, weights W , bias b
3: Cost function $E(\mathbf{X}, \hat{\mathbf{X}}, \Phi_{W,b})$
4: Derivative function by backpropagation δ
5: Optimizer function of the gradient $g(\mathbf{x})$
6: Max number of epochs I_{\max}
7: Initialize $W, b \leftarrow$ random numbers
8: **for** $k \leftarrow 1$ to I_{\max} **do**
9: /* Propagate forward MLP in training dataset */
10: **for all** training data $(\mathbf{x}, y) \in \mathbf{X}$ **do**
11: $\mathbf{e}_1 \leftarrow y - \Phi_{W,b}(\mathbf{x})$
12: **end for**
13: /* Calculate the derivatives of MLP in mesh grid points */
14: **for all** mesh grid point $\hat{\mathbf{x}} \in \hat{\mathbf{X}}$ **do**
15: $\mathbf{e}_2, \mathbf{e}_3 \leftarrow \nabla \Phi_{W,b}(\hat{\mathbf{x}}), \nabla^2 \Phi_{W,b}(\hat{\mathbf{x}})$
16: **end for**
17: /* Calculate the total cost */
18: $\mathbf{e}_4 \leftarrow E(\mathbf{X}, \hat{\mathbf{X}}, \Phi_{W,b})$
19: /* Calculate partial derivatives with respect to parameters
20: of the cost function by backpropagation */
21: $\frac{\partial E}{\partial W}, \frac{\partial E}{\partial b} \leftarrow \delta_W E, \delta_b E$
22: /* Update the weights and bias */
23: $W, b \leftarrow W - g\left(\frac{\partial E}{\partial W}\right), b - g\left(\frac{\partial E}{\partial b}\right)$
24: **end for**
25: **return** $\Phi_{W,b}, \mathbf{e}$

Algorithm 1 exhibits characteristics that set it apart from conventional learning methods. First, the computation points $\hat{\mathbf{X}}$ for the derivatives of the MLP do not correspond with the points of the training dataset \mathbf{X} , which is typically sparse and unbalanced. The algorithm adjusts the derivatives to fit mesh grids, hence capturing derivative data across a wide array of input features. Secondly, the cost function E does not depend only on the MLP's direct output

but also on its derivatives as specified in Eq.(9), all of which depend on identical network parameters. DCNN facilitates accurate calibration and gradient computation of the parameters through precise formulations, which consist of a linear transformation and the activation function's derivatives, as described in the previous section.

5 TESTING WITH SYNTHETIC DATA

The developed algorithm (i.e. DCNN) for evaluating volatility smile and skewness was first tested on simulated values in a parameterized two-dimensional case of the surface interpolation problem. We took up the well-known Stochastic Alpha Beta Rho (SABR) model [22] and prepared a sparse two-dimensional dataset to test our methodology. As an empirical experiment, we applied DCNN for the surface interpolation with real market data, which are sparse, and examined the efficiency of the solution for the surface with no-arbitrage constraints.

5.1 The SABR model

The SABR model [22] is a typical parametric model, which can capture the market volatility smile and skewness and reasonably depict market structure. When F_t is defined as the forward price of an underlying asset at time t , the SABR model is described as

$$\begin{aligned}dF_t &= \alpha_t F_t^\beta dW_t^1, \\ d\alpha_t &= v \alpha_t dW_t^2, \\ \langle dW_t^1, dW_t^2 \rangle &= \rho dt.\end{aligned}\quad (13)$$

Here, W_t^1, W_t^2 are standard Wiener processes, α_t is the model volatility, ρ is the correlation between the two processes, and v is analogous to vol of vol in the Heston model, these are parameters corresponding to skewness and smiles. The additional parameter β describes the slope of the skewness. A significant feature of the SABR model is that the price of the European option can be formulated in closed form, as shown in [22], up to the accuracy of a series expansion. Essentially it is shown there that the IV in the SABR model is given by the appropriate Black formula in [6, 22]. For given α, β, ρ, v and $F = S_t e^{r\tau}$ with a fixed risk-free rate under the risk-neutral measure in [27], this volatility is given by:

$$\begin{aligned}\sigma_{\text{SABR}}(K, \tau) &= \frac{\alpha \left(1 + \left(\frac{(1-\beta)^2}{24} \frac{\alpha^2}{(FK)^{1-\beta}} + \frac{1}{4} \frac{\rho \beta v \alpha}{(FK)^{(1-\beta)/2}} + \frac{2-3\rho^2}{24} v^2 \right) \tau \right)}{(FK)^{(1-\beta)/2} \left[1 + \frac{(1-\beta)^2}{24} \ln^2 \frac{F}{K} + \frac{(1-\beta)^4}{1920} \ln^4 \frac{F}{K} \right]} \frac{z}{\chi(z)}, \\ z &= \frac{v}{\alpha} (FK)^{(1-\beta)/2} \ln \frac{F}{K}, \quad \chi(z) = \ln \left(\frac{\sqrt{1-2\rho z+z^2} + z - \rho}{1-\rho} \right).\end{aligned}\quad (14)$$

Note as in [22] that if $K = F$ then the z and $\chi(z)$ terms are removed from the equation, as then $\frac{z}{\chi(z)} = 1$ in the sense of a limit, and so

$$\sigma_{\text{SABR}}(F, \tau) = \frac{\alpha \left(1 + \left(\frac{(1-\beta)^2}{24} \frac{\alpha^2}{F^{2-2\beta}} + \frac{1}{4} \frac{\rho \beta v \alpha}{F^{1-\beta}} + \frac{2-3\rho^2}{24} v^2 \right) \tau \right)}{F^{1-\beta}}. \quad (15)$$

Discussion and analysis of parameters setting methodologies for the SABR model with limited input data is also discussed in [51].

Finally, Option premiums for the experiment are computed from the volatility σ_{SABR} by the Black formula [6]. This is similar to the Black-Scholes formula [7] for valuing options, except that the underlying spot price is replaced by a discounted forward price F . Then the Black formula states the price for a European call option is

$$C(K, \tau) = e^{-r\tau} [FN(d_1) - KN(d_2)], \quad (16)$$

where

$$d_1 = \frac{\ln(F/K) + (\sigma_{\text{SABR}}^2/2)\tau}{\sigma\sqrt{\tau}}, \quad d_2 = d_1 - \sigma_{\text{SABR}}\sqrt{\tau}, \quad (17)$$

and $N(\cdot)$ is the cumulative normal distribution function.

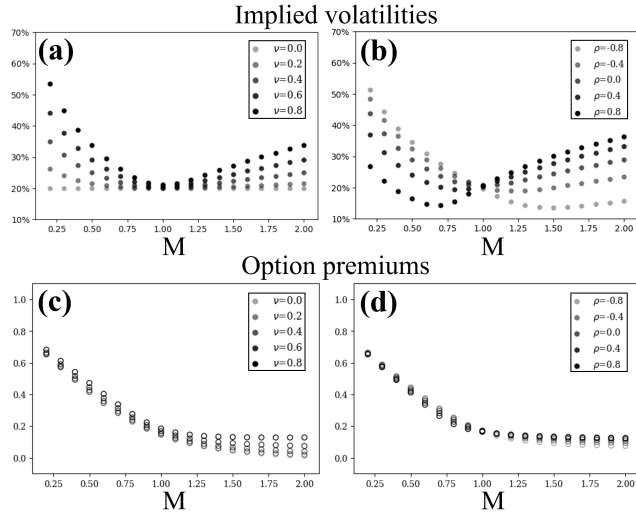


Figure 3: Sparse data of implied volatility (IV) and option (call) premiums using the Stochastic Alpha Beta Rho (SABR) model by moneyness $M = K/F$. (a) The volatilities by smile parameters (v) with fixed $\rho = 0$. (b) By skewness parameters (ρ) with fixed $v = 0.6$. (c-d) shows the option (call) premiums with corresponding to (a-b).

It is noted that option characteristics are often encapsulated in IV, but the market variables are option premiums. Figure 3 shows the volatilities and premiums under fixed parameters by $F = 1$, $\alpha = 0.2$, $\beta = 1$, $r = 0.04$, $\tau = 1$, and $M = K/F$. By changing smile and skewness parameters, we observe a smaller difference in the numerical values on a premium basis in Figure 3 (c-d) than that of volatility in Figure 3 (a-b). Therefore, the calibration task in the actual situation becomes a challenging problem to capture smile and skewness characteristics based on the observed premiums.

5.2 Experimental design

To investigate the ability of ANNs to recreate the volatility smile and skewness, we prepared sparse option premiums for in-sample testing and dense ones for out-of-sample testing based on the SABR model. Sparse option premiums used for in-sample testing are calculated using mesh grids by 25 points for $M = K/F \in [0.1, 2.5]$ and 7 for $T \in [0.1, 0.5, 1, 2, 3, 4, 5]$ with varying smile (v) and skewness

(ρ) parameters. Additionally, samples contain the boundary conditions with 200 additional points with $M \in [0, 2.5]$ and $\tau = 0$ or in $T \in [0, 5]$ and $K = 0$. After that, these premiums are fitted into various models, such as the cubic spline method, MLP, and DCNN. For comparison, we evaluate the errors from the predictions using dense mesh grids as out-of-sample, which are equally distributed by 126 points in $M \in [0, 2.5]$ and 51 in $T \in [0, 5]$. We use an evaluation metric as followability of smile and skewness as similar to Eq (5),

$$E_{\text{MSE}}^{(\sigma)} = \frac{1}{N} \sum_{i=1}^N \{\sigma_{\text{SABR}}(K_i, \tau_i) - \sigma_{\text{Black}}(\Phi(K_i, \tau_i), F, K_i, r, \tau_i)\}^2, \quad (18)$$

where $\sigma_{\text{Black}}(\cdot)$ is the function which computes IV based on the Black model [6] corresponding to the predicted premium $\Phi(K_i, \tau_i)$.

The base MLP architecture used in this study consists of two fully connected hidden layers with Softplus activation functions, whose derivatives are $f' : (1 + e^{-x})^{-1}$, $f'' : e^{-x}(1 + e^{-x})^{-2}$ in Eqs. (11) and (12), with an output layer with a linear function (i.e. no activation function). Each layer has 16 neurons. We set the number of epochs as 10,000, and Adam [33] as the optimizer using gradient-based training with normally randomised weight initialization. In the cubic spline model, we use the SmoothBivariateSpline function with three degrees in the Scipy package [50] in Python. Our numerical experiments were run using Pytorch [39] and JAX [8] packages for efficient automatic differentiation on Google Colaboratory [20] with 36 GB of RAM and a dual-core CPU of 2.3 GHz. We consistently used the same random seeds across different conditions for the statistical analysis and changed these seed values ten times. We set $m_1 = m_3 = 0.001$, $m_2 = 0.01$, $g(x) = x$ in Eq. (6), and $\alpha = 0.2$, $\beta = 1.0$, and $r = 0.04$ as the parameters of the SABR model. The visualizations in the figures of the results section were based on the model outputs when $v = 0.6$ and $\rho = -0.4$.

5.3 The S&P 500 dataset

The empirical experiments were conducted using intraday prices for S&P 500 call options from 10th to 14th July 2023; we obtained about two thousand points on a daily basis via the Yahoo finance library as Table 1. We added the synthesized points corresponding to boundary conditions to training, and all other setups are the same as in the previous section.

Table 1: A summary of intraday prices for S&P 500 options.

	10-Jul-23	11-Jul-23	12-Jul-23	13-Jul-23	14-Jul-23
count	2,066	1,930	2,261	1,757	1,963
τ_{min}	0.005	0.000	0.000	0.000	0.000
τ_{max}	5.444	4.438	5.433	5.430	5.427
M_{min}	0.022	0.022	0.041	0.043	0.042
M_{max}	2.312	2.310	2.297	1.939	1.926

5.4 Results

We obtained sparse in-sample data for training and dense out-of-sample data to compare the effectiveness of interpolation with volatility smile and skewness by models: cubic spline, MLP, and DCNN.

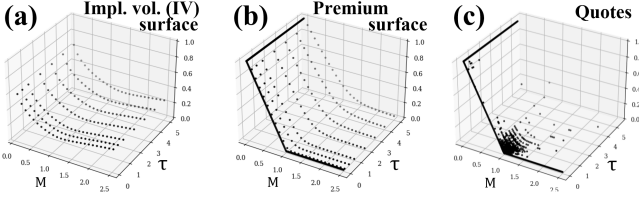


Figure 4: Sparse samples for the training set. (a) The IVs with the fixed SABR parameter ($\nu = 0.6, \rho = -0.4$). (b) the option premiums corresponding to (a) with initial and boundary conditions in Eq.(2). (c) S&P 500 option premiums traded intra-day as of 12th July 2023, with boundary conditions.

At first, we show the issue associated with generating the IV surface near boundary conditions. As shown in 4(a), we can prepare the whole volatility surface using the SABR model; however, the original option premiums in Figure 4 (c) largely comprise of at-the-money options with a short time to expiry which makes it is hard to identify a complete implied volatility surface from premiums.

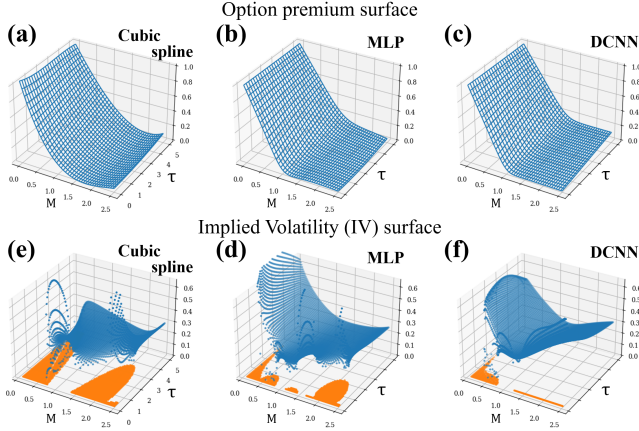


Figure 5: Calibrated models fitted by synthesized option premiums via SABR model (a-c), and IV surface completed by those premiums (d-f). Orange points show the invalid IVs computed by corresponding to option premiums (a-c).

Figure 5 (a-c) illustrates the predicted results for option premiums from trained models derived from out-of-sample data. In Figure 5(e-f), we compare the profiles of the IV surface created by the cubic spline method, MLP, and DCNN. Training times were approximately 30 seconds for a simple MLP and 50 for DCNN. Note again that calibration provided option premium surfaces, which were converted to the implied volatility surface. As a result, the cubic spline method, a simple interpolation approach, reveals the largest area of invalid volatility, signifying a higher IV error. In contrast, more sophisticated techniques, like MLP and particularly DCNN, display fewer errors. Additionally, DCNN gives the most stable results for IV, indicating that it effectively generates a surface that can represent smile and skewness features, thus characterizing the IV surface more precisely.

Table 2: Premium and volatility errors in out-of-sample. **Bold** values indicate lower (better) values among the models.

Conditions		Out-of-sample Errors					
SABR param.		Cubic Spline		MLP		DCNN	
ν	ρ	E_{MSE} $\times 10^{-4}$	$E_{\text{MSE}}^{(\sigma)}$ $\times 10^{-2}$	E_{MSE} $\times 10^{-4}$	$E_{\text{MSE}}^{(\sigma)}$ $\times 10^{-2}$	E_{MSE} $\times 10^{-4}$	$E_{\text{MSE}}^{(\sigma)}$ $\times 10^{-2}$
0.0	0.0	6.24	2.58	0.29	1.99	0.32	1.36
0.2	0.0	6.25	2.78	0.28	1.99	0.29	1.39
0.4	0.0	6.28	3.15	0.30	1.98	0.28	1.51
0.6	0.0	6.39	3.65	0.29	1.95	0.26	1.56
0.8	0.0	6.65	4.21	0.32	1.97	0.28	1.57
0.6	-0.8	6.78	4.45	0.31	2.03	0.26	1.63
0.6	-0.4	6.77	4.61	0.30	1.99	0.25	1.63
0.6	0.4	6.83	4.57	0.30	1.97	0.25	1.63
0.6	0.8	7.02	4.41	0.33	1.98	0.28	1.61

To corroborate the assumption, we tabulated the prediction errors in Eqs. (5) and (18), which signify the predicted option premiums and their IV on the mesh grid for out-of-sample data, in contrast with the ideal values calculated by the SABR model. These errors are summarized in Table 2. It is clear that the cubic spline method displays the highest errors in both metrics in all cases. In contrast, MLP and DCNN perform similarly with regard to the premium, while DCNN performs better for volatility. This variation in MLP and DCNN performance across different metrics suggests that DCNN is more efficient in recognizing features on the IV surface, likely due to its integration of no-arbitrage constraints.

Table 3: In-sample errors in accuracy and penalty losses. **Bold** values indicate lower (better) values among the models.

Conditions		In-sample Errors					
SABR param.		Cubic Spline		MLP		DCNN	
ν	ρ	E_{MSE} $\times 10^{-4}$	$E_{\mathcal{P}}$ $\times 10^{-3}$	E_{MSE} $\times 10^{-4}$	$E_{\mathcal{P}}$ $\times 10^{-3}$	E_{MSE} $\times 10^{-4}$	$E_{\mathcal{P}}$ $\times 10^{-3}$
0.0	0.0	8.44	415.0	0.47	0.38	1.85	0.13
0.2	0.0	8.44	414.8	0.39	0.32	1.64	0.12
0.4	0.0	8.45	414.1	0.46	0.34	1.65	0.11
0.6	0.0	8.48	412.6	0.45	0.36	1.57	0.11
0.8	0.0	8.55	410.2	0.46	0.35	1.48	0.10
0.6	-0.8	8.59	407.9	0.45	0.34	1.42	0.09
0.6	-0.4	8.59	406.6	0.43	0.33	1.36	0.09
0.6	0.4	8.60	408.4	0.43	0.33	1.38	0.09
0.6	0.8	8.65	411.3	0.46	0.34	1.46	0.10
Quotes 10Jul23		5.75	125.9	0.30	0.67	3.99	0.34
Quotes 11Jul23		5.67	114.2	0.48	0.64	3.92	0.34
Quotes 12Jul23		5.52	119.4	0.50	0.90	3.91	0.33
Quotes 13Jul23		6.01	150.2	0.35	0.78	3.86	0.34
Quotes 14Jul23		6.05	166.6	1.46	1.15	5.38	0.35

Next, in Table 3, we also analyzed the errors in Eqs. (5) and (6), representing calibration performance of option premiums and derivatives implied by the no-arbitrage conditions. While MLP

offered the best results in the premium metric, DCNN excelled in the risk metric. This different performance of MLP and DCNN across different metrics substantiates the idea that DCNN's superior capability for identifying features on the IV surface is likely due to its integration of no-arbitrage constraints during learning.

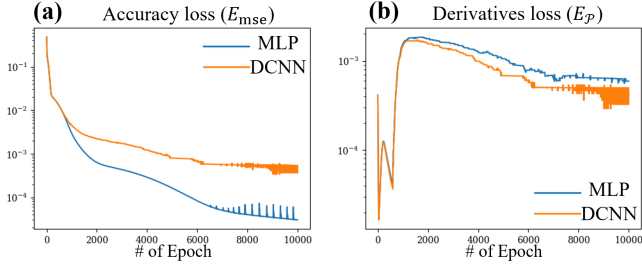


Figure 6: The accuracy (MSE) (a) and loss due to the derivatives (b) with a logarithmic scale by learning epochs.

Furthermore, Figure 6 depicts the MSE loss and the penalty loss due to derivative terms across various epochs. A trade-off between solution accuracy and the penalty from derivative terms is visible throughout the learning process. In Figure 6(b), a decrease in penalty related to the derivative term is seen for DCNNs. This trend shows a trade-off between accuracy and penalty from derivative terms, brought about by the effort to comply with no-arbitrage constraints during learning.

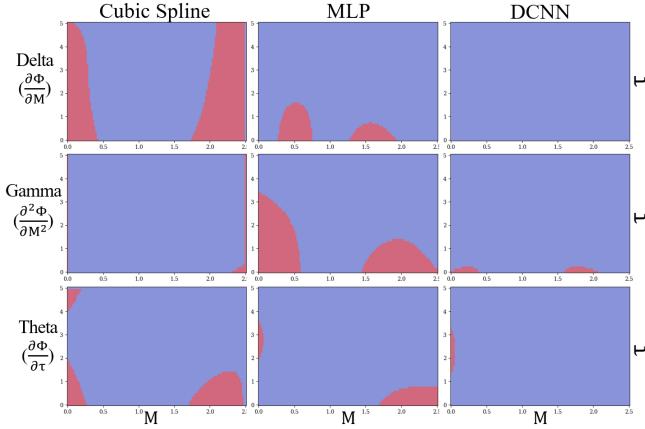


Figure 7: Risk profiles (i.e. derivative terms) comparison by option premium surface. The red-coloured area indicates breaking no-arbitrage conditions.

Lastly, Figure 7 shows the first and second differentials of predicted values in M and τ in Eq. (3). DCNN effectively ensures that the results do not infringe on the conditions for derivative values, each of which aligns with an inequality constraint in Eq. (3). In Figure 7, we see that the plots for DBP have fewer areas in red denoting the regions where the no-arbitrage conditions on the derivatives are broken. Consequently, these findings prove that DCNN is a powerful tool that aids practitioners not only in understanding market volatility dynamics but also in managing risks effectively.

6 DISCUSSION

The specific contributions of this paper are as follows:

- (1) The development of a new calibration framework for option premiums: This study utilized the DCNN algorithm, powered by deep learning, which efficiently computes derivatives with automatic differentiation and introduces differential constraints, allowing convergence to the appropriate function surface with accurate detection of volatility characteristics whilst adhering to no-arbitrage conditions.
- (2) Effectiveness of DCNN in capturing the features of the IV surface: The study utilized the SABR model to assess the ability of DCNN to represent the capability of smile and skewness features in IV surfaces. DCNN significantly improved the interpolation of the premium surface for volatility smile and skewness due to deep learning with no-arbitrage constraints.
- (3) Trade-offs between price accuracy and derivative penalty: The findings demonstrate that as the learning process proceeds, there's a decrease in the penalty associated with the derivative term, reflecting a balance between accuracy and penalty from derivative terms. The results emphasize the network's efforts to comply with no-arbitrage constraints during learning, enhancing the model's overall effectiveness and robustness.

7 CONCLUSION

This paper presents a novel financial application using Derivative-Constrained Neural Networks (DCNN) in a neural network algorithm for approximating solutions to partial differential equations. It employs derivative values obtained through automatic differentiation, enhancing the overall accuracy and interpretability of the solution. This includes meeting constraints such as no-arbitrage and capturing volatility smile and skewness effects, which addresses the limitations of traditional calibration methods in scenarios with sparse training data. Consequently, in our experimental setup, DCNN demonstrated superior performance in identifying features on the implied volatility surface, likely due to its incorporation of no-arbitrage constraints during the learning process. The research uses the Stochastic Volatility model to showcase the improved interpolation of the premium surface and risk profiles. The findings highlight the potential of DCNN as a tool for understanding market dynamics and managing risk. It provides a data-driven solution to calibration problems, allowing for an accurate representation of volatility characteristics.

REFERENCES

- [1] Damien Ackerer, Natasa Tagasovska, and Thibault Vatter. 2020. Deep smoothing of the implied volatility surface. *Advances in Neural Information Processing Systems* 33 (2020), 11552–11563.
- [2] Yacine Ait-Sahalia and Jefferson Duarte. 2003. Nonparametric option pricing under shape restrictions. *Journal of Econometrics* 116, 1-2 (2003), 9–47.
- [3] Jacob Barhak and Anath Fischer. 2001. Parameterization and reconstruction from 3D scattered points based on neural network and PDE techniques. *IEEE Transactions on visualization and computer graphics* 7, 1 (2001), 1–16.
- [4] Christian Bayer, Blanka Horvath, Aitor Muguruza, Benjamin Stemper, and Mehdi Tomas. 2019. On deep calibration of (rough) stochastic volatility models. *arXiv preprint arXiv:1908.08806* (2019).
- [5] Maxime Bergeron, Nicholas Fung, John Hull, Zisis Poulos, and Andreas Veneris. 2022. Variational autoencoders: A hands-off approach to volatility. *The Journal of Financial Data Science* 4, 2 (2022), 125–138.
- [6] Fischer Black. 1976. The pricing of commodity contracts. *Journal of financial economics* 3, 1-2 (1976), 167–179.

[7] Fischer Black and Myron Scholes. 1973. The pricing of options and corporate liabilities. *Journal of political economy* 81, 3 (1973), 637–654.

[8] James Bradbury, Roy Frostig, Peter Hawkins, Matthew James Johnson, Chris Leary, Dougal Maclaurin, George Necula, Adam Paszke, Jake VanderPlas, Skye Wanderman-Milne, and Qiao Zhang. 2018. JAX: composable transformations of Python+NumPy programs. <http://github.com/google/jax>

[9] Yi Cao, Xiaoquan Liu, and Jia Zhai. 2021. Option valuation under no-arbitrage constraints with neural networks. *European Journal of Operational Research* 293, 1 (2021), 361–374.

[10] Peter Carr and Dilip B Madan. 2005. A note on sufficient conditions for no arbitrage. *Finance Research Letters* 2, 3 (2005), 125–130.

[11] Ricky TQ Chen, Yulia Rubanova, Jesse Bettencourt, and David K Duvenaud. 2018. Neural ordinary differential equations. *Advances in neural information processing systems* 31 (2018).

[12] Vedant Choudhary, Sebastian Jaimungal, and Maxime Bergeron. 2023. FuVol: A Multi-Asset Implied Volatility Market Simulator using Functional Principal Components and Neural SDEs. *arXiv preprint arXiv:2303.00859* (2023).

[13] Rama Cont and Milena Vuletić. 2022. Simulation of arbitrage-free implied volatility surfaces. *Available at SSRN* (2022).

[14] Charles J Corrado and Tie Su. 1997. Implied volatility skews and stock index skewness and kurtosis implied by S&P 500 index option prices. *Journal of Derivatives* 4, 4 (1997), 8–19.

[15] George Cybenko. 1989. Approximation by superpositions of a sigmoidal function. *Mathematics of control, signals and systems* 2, 4 (1989), 303–314.

[16] Freddy Delbaen and Walter Schachermayer. 1994. A general version of the fundamental theorem of asset pricing. *Mathematische annalen* 300, 1 (1994), 463–520.

[17] Emanuel Derman, Iraj Kani, and Joseph Z Zou. 1996. The local volatility surface: Unlocking the information in index option prices. *Financial analysts journal* 52, 4 (1996), 25–36.

[18] Bruno Dupire et al. 1994. Pricing with a smile. *Risk* 7, 1 (1994), 18–20.

[19] Matthias R Fengler and Lin-Yee Hin. 2015. Semi-nonparametric estimation of the call-option price surface under strike and time-to-expiry no-arbitrage constraints. *Journal of Econometrics* 184, 2 (2015), 242–261.

[20] Google. 2023. Frequently Asked Questions. Available online: <https://research.google.com/collaboratory/faq.html> (accessed on 24th Jul 2023) (2023).

[21] Nyoman Gunantara. 2018. A review of multi-objective optimization: Methods and its applications. *Cogent Engineering* 5, 1 (2018), 1502242.

[22] Patrick S Hagan, Deep Kumar, Andrew S Lesniewski, and Diana E Woodward. 2002. Managing smile risk. *The Best of Wilmott* 1 (2002), 249–296.

[23] Steven L Heston. 1993. A closed-form solution for options with stochastic volatility with applications to bond and currency options. *The review of financial studies* 6, 2 (1993), 327–343.

[24] Kurt Hornik, Maxwell Stinchcombe, and Halbert White. 1989. Multilayer feed-forward networks are universal approximators. *Neural networks* 2, 5 (1989), 359–366.

[25] Kurt Hornik, Maxwell Stinchcombe, and Halbert White. 1990. Universal approximation of an unknown mapping and its derivatives using multilayer feedforward networks. *Neural networks* 3, 5 (1990), 551–560.

[26] Blanka Horvath, Aitor Muguruza, and Mehdi Tomas. 2021. Deep learning volatility: a deep neural network perspective on pricing and calibration in (rough) volatility models. *Quantitative Finance* 21, 1 (2021), 11–27.

[27] John Hull. 1993. *Options, futures, and other derivative securities*. Vol. 7. Prentice Hall Englewood Cliffs, NJ.

[28] John Hull and Alan White. 1990. Pricing interest-rate-derivative securities. *The review of financial studies* 3, 4 (1990), 573–592.

[29] Andrey Itkin. 2019. Deep learning calibration of option pricing models: some pitfalls and solutions. *arXiv preprint arXiv:1906.03507* (2019).

[30] Huisu Jang and Jaewook Lee. 2019. Generative Bayesian neural network model for risk-neutral pricing of American index options. *Quantitative Finance* 19, 4 (2019), 587–603.

[31] Alex Kendall, Yarin Gal, and Roberto Cipolla. 2018. Multi-task learning using uncertainty to weigh losses for scene geometry and semantics. In *Proceedings of the IEEE conference on computer vision and pattern recognition*, 7482–7491.

[32] Yuehaw Khoo, Jianfeng Lu, and Lexing Ying. 2021. Solving parametric PDE problems with artificial neural networks. *European Journal of Applied Mathematics* 32, 3 (2021), 421–435.

[33] Diederik P Kingma and Jimmy Ba. 2014. Adam: A method for stochastic optimization. *arXiv preprint arXiv:1412.6980* (2014).

[34] Sören Laue, Matthias Mitterreiter, and Joachim Giesen. 2020. A simple and efficient tensor calculus. In *Proceedings of the AAAI Conference on Artificial Intelligence*, Vol. 34, 4527–4534.

[35] Shuaiqiang Liu, Anastasia Borovykh, Lech A Grzelak, and Cornelis W Oosterlee. 2019. A neural network-based framework for financial model calibration. *Journal of Mathematics in Industry* 9 (2019), 1–28.

[36] KaiChieh Lo and Daniel Huang. 2023. On Training Derivative-Constrained Neural Networks. *arXiv:cs.LG/2310.01649*

[37] Pablo Márquez-Neila, Mathieu Salzmann, and Pascal Fua. 2017. Imposing hard constraints on deep networks: Promises and limitations. *arXiv preprint arXiv:1706.02025* (2017).

[38] William McGhee. 2020. An artificial neural network representation of the SABR stochastic volatility model. *Journal of Computational Finance* 25, 2 (2020).

[39] Adam Paszke, Sam Gross, Francisco Massa, Adam Lerer, James Bradbury, Gregory Chanan, Trevor Killeen, Zeming Lin, Natalia Gimelshein, Luca Antiga, Alban Desmaison, Andreas Kopf, Edward Yang, Zachary DeVito, Martin Raison, Alykhan Tejani, Sasank Chilamkurthy, Benoit Steiner, Lu Fang, Junjie Bai, and Soumith Chintala. 2019. PyTorch: An Imperative Style, High-Performance Deep Learning Library. In *Advances in Neural Information Processing Systems* 32. Curran Associates, Inc., 8024–8035. <http://papers.neurips.cc/paper/9015-pytorch-an-imperative-style-high-performance-deep-learning-library.pdf>

[40] Jaime Pizarroso, José Portela, and Antonio Muñoz. 2020. NeuralSens: sensitivity analysis of neural networks. *arXiv preprint arXiv:2002.11423* (2020).

[41] Maziar Raissi, Paris Perdikaris, and George E Karniadakis. 2019. Physics-informed neural networks: A deep learning framework for solving forward and inverse problems involving nonlinear partial differential equations. *Journal of Computational physics* 378 (2019), 686–707.

[42] Robert Reams. 1999. Hadamard inverses, square roots and products of almost semidefinite matrices. *Linear Algebra Appl.* 288 (1999), 35–43.

[43] Michael Roper. 2010. Arbitrage free implied volatility surfaces. *preprint* (2010).

[44] Mark Rubinstein. 1985. Nonparametric tests of alternative option pricing models using all reported trades and quotes on the 30 most active CBOE option classes from August 23, 1976 through August 31, 1978. *The Journal of Finance* 40, 2 (1985), 455–480.

[45] Johannes Ruf and Weiguan Wang. 2019. Neural networks for option pricing and hedging: a literature review. *arXiv preprint arXiv:1911.05620* (2019).

[46] David E Rumelhart, Geoffrey E Hinton, and Ronald J Williams. 1986. Learning representations by back-propagating errors. *nature* 323, 6088 (1986), 533–536.

[47] Bert Speelpenning. 1980. *Compiling fast partial derivatives of functions given by algorithms*. University of Illinois at Urbana-Champaign.

[48] Gjorgji Strezoski and Marcel Worring. 2017. Omnia: multi-task deep learning for artistic data analysis. *arXiv preprint arXiv:1708.00684* (2017).

[49] Stefan Van Der Walt, S Chris Colbert, and Gael Varoquaux. 2011. The NumPy array: a structure for efficient numerical computation. *Computing in science & engineering* 13, 2 (2011), 22–30.

[50] Pauli Virtanen, Ralf Gommers, Travis E Oliphant, Matt Haberland, Tyler Reddy, David Cournapeau, Evgeni Burovski, Pearu Peterson, Warren Weckesser, Jonathan Bright, et al. 2020. SciPy 1.0: fundamental algorithms for scientific computing in Python. *Nature methods* 17, 3 (2020), 261–272.

[51] Graeme West. 2005. Calibration of the SABR model in illiquid markets. *Applied Mathematical Finance* 12, 4 (2005), 371–385.

[52] Zhiwei Yao, Amir Gholami, Kurt Keutzer, and Michael W Mahoney. 2020. PyHessian: Neural networks through the lens of the hessian. In *2020 IEEE international conference on big data (Big data)*. IEEE, 581–590.

[53] I-Cheng Yeh and Wei-Lun Cheng. 2010. First and second order sensitivity analysis of MLP. *Neurocomputing* 73, 10–12 (2010), 2225–2233.

[54] Cha Zhang and Zhengyou Zhang. 2014. Improving multiview face detection with multi-task deep convolutional neural networks. In *IEEE Winter Conference on Applications of Computer Vision*. IEEE, 1036–1041.

A THE FIRST AND SECOND DERIVATIVES OF MULTI-LAYER PERCEPTRON (MLP)

This section extends the work on the first and second derivatives of MLP to cross derivatives. In second derivative calculations, Eq. (12) can be applied for the selections of second-order partial derivatives, but not for the mixed partial derivatives. Following the notation in Section 4, we can redefine ∇^2 in Eq. (10) with cross derivatives using the Hessian matrix,

$$\nabla^2 \Phi_{W,b}(\mathbf{x}) := \mathbf{H}_\Phi = \begin{bmatrix} \frac{\partial^2 \Phi}{\partial x_1^2} & \frac{\partial^2 \Phi}{\partial x_1 \partial x_2} & \cdots & \frac{\partial^2 \Phi}{\partial x_1 \partial x_n} \\ \frac{\partial^2 \Phi}{\partial x_2 \partial x_1} & \frac{\partial^2 \Phi}{\partial x_2^2} & \cdots & \frac{\partial^2 \Phi}{\partial x_2 \partial x_n} \\ \vdots & \ddots & \ddots & \vdots \\ \frac{\partial^2 \Phi}{\partial x_n \partial x_1} & \frac{\partial^2 \Phi}{\partial x_n \partial x_2} & \cdots & \frac{\partial^2 \Phi}{\partial x_n^2} \end{bmatrix}. \quad (19)$$

Here, the entry of the i -th row and the j -th column is

$$\left(\mathbf{H}_f\right)_{ij} = \frac{\partial^2 f}{\partial x_i \partial x_j}. \quad (20)$$

Similarly, we reconsider the second derivative of each layer $\nabla_l^2 \in \mathbb{R}^{d_l \times n \times n}$ at the l -th layer defined in Eq. (12) with cross derivatives,

$$\nabla_l^2 := \frac{\partial^2 \mathbf{x}_l}{\partial \mathbf{x}^2} = \left[\mathbf{H}_{x_1^{(l)}}, \dots, \mathbf{H}_{x_{d_l}^{(l)}} \right] \quad (21)$$

where, the elements of the Hessian matrix $\mathbf{H}_{x_i^{(l)}}$ are

$$\mathbf{H}_{x_i^{(l)}} = \begin{bmatrix} \frac{\partial^2 x_i^{(l)}}{\partial x_1^2} & \dots & \frac{\partial^2 x_i^{(l)}}{\partial x_1 \partial x_n} \\ \vdots & \ddots & \vdots \\ \frac{\partial^2 x_i^{(l)}}{\partial x_n \partial x_1} & \dots & \frac{\partial^2 x_i^{(l)}}{\partial x_n^2} \end{bmatrix}. \quad (22)$$

Calculating the derivatives of tensor equations, a process known as tensor calculus, is crucial in machine learning. One significant aspect to consider is the efficiency of evaluating these equations and their derivatives, which depends on the way these expressions are represented. Here, Eqs. (11) and (12) - which contain cross derivatives and are characterized by tensor computations in an automatic differentiation framework.

Tensor calculation [34]. In tensor calculus, for tensors A, B , and C the multiplication of A and B can be written as

$$C[s_3] = \sum_{(s_1 \cup s_2) \setminus s_3} A[s_1] \cdot B[s_2] = A *_{(s_1, s_2, s_3)} B \quad (23)$$

where C is the result tensor and s_1, s_2 , and s_3 are the index sets of the left argument, the right argument, and the result tensor, respectively. The summation index is excluded from the index set of the result tensor $s_3 \subseteq (s_1 \cup s_2)$ explicitly represents the index set of C , which is always a subset of the union of s_1 and s_2 .

Based on the definition provided, tensor multiplication can be described succinctly with fewer summation symbols. Furthermore, this notation closely resembles the tensor multiplication *einsum* found in Python packages. As an illustration, the inner product of matrices A and B can be expressed as

$$A *_{(i, k, j, i)} B = \sum_k A_{ik} \cdot B_{kj} = A \cdot B. \quad (24)$$

Subsequently, we present a formulation for the first and second derivatives of the function Φ . Note that the product chain rule can be employed between the l -th and $(l-1)$ -th layers, given that each layer is fully connected in the feedforward network.

Initially, we examine the first-order derivatives of each layer's output \mathbf{x}_l with respect to the input features \mathbf{x} . Note that the input features are $\mathbf{x} \in \mathbb{R}^n$ and $\mathbf{x} = x_1, \dots, x_n$. The outputs of the l -th layer are denoted as $\mathbf{x}^{(l)} \in \mathbb{R}^{d_l}$, where $\mathbf{x}^{(l)} = x_1^{(l)}, \dots, x_{d_l}^{(l)}$. Consequently, each element of the first derivative at the first layer is formulated as

$$\frac{\partial x_j^{(1)}}{\partial x_i} = (f'_1 \circ A_1(\mathbf{x}))_j \times (W_1^\top)_{ji}. \quad (25)$$

By employing tensor calculation, we can succinctly represent

$$(\nabla_1)_{ji} = \frac{\partial x_j^{(1)}}{\partial x_i} \text{ as}$$

$$\nabla_1 = f'_1 \circ A_1(\mathbf{x}) *_{(j, ji, ji)} W_1^\top, \quad (26)$$

For $l = 2, \dots, L-1$, we adhere to the linear algebra notations found in [34], and rewrite Eq. (11) using tensor notation with the chain product rule

$$\nabla_l = \left\{ (f'_l \circ A_l(\mathbf{x}_{l-1})) *_{(j, ji, ji)} W_l^\top \right\} \nabla_{l-1}. \quad (27)$$

∇_l is expressed because the last layer lacks an activation function,

$$\nabla_L = \{A_L(\mathbf{x}_{L-1}) *_{(j, ji, ji)} W_L^\top\} \nabla_{L-1}. \quad (28)$$

Correspondingly, leveraging the above equations, we can formulate the second derivatives with cross derivatives. At this juncture, each element of the second derivative at the first layer is formulated as

$$\mathbf{H}_{x_j^{(1)}} = \left(f''_1 \circ A_1(\mathbf{x}) *_{(j, ji, ji)} (W_1^\top) \right)_j \otimes (W_1^\top)_j, \quad (29)$$

where \otimes indicates the dyadic product of vectors. Utilizing the tensor calculation, we can represent $(\nabla_1^2)_j = \mathbf{H}_{x_j^{(1)}}$ as

$$\nabla_1^2 = \{f''_1 \circ A_1(\mathbf{x}) *_{(j, ji, ji)} (W_1^\top)\} *_{(j, jk, jk)} (W_1^\top). \quad (30)$$

When $l = 2, \dots, L-1$, the partial derivatives of the outputs of the l -th layer with respect to \mathbf{x} is calculated using the product rule, i.e. $(u \cdot v)' = u' \cdot v + u \cdot v'$, for Eq. (27) with ∇_{l-1} and ∇_{l-1}^2 as

$$\begin{aligned} \nabla_l^2 = & \left\{ f''_l \circ A_l(\mathbf{x}_{l-1}) *_{(j, ji, ji)} (W_l^\top \nabla_{l-1}) \right\} *_{(j, jk, jk)} (W_l^\top \nabla_{l-1}) \\ & + \{f'_l \circ A_l(\mathbf{x}_{l-1}) *_{(j, ji, ji)} W_l^\top\} *_{(jm, mik, jik)} \nabla_{l-1}^2, \end{aligned} \quad (31)$$

where f'_l and f''_l are the first and second-order derivatives of the activation function at the l -th layer, respectively. Lastly, the second derivative for the last layer, which is equivalent to $\nabla^2 \Phi(\mathbf{x})$, is obtained as

$$\nabla^2 \Phi(\mathbf{x}) = \nabla_L^2 = \{A_L(\mathbf{x}_{L-1}) *_{(j, ji, ji)} W_L^\top\} *_{(jm, mik, jik)} \nabla_{L-1}^2. \quad (32)$$

The second-order derivatives with cross derivatives of an MLP, as delineated in Eq. (32), can be seamlessly integrated into Algorithm 1. When applying Eq. (32) with input features $\mathbf{x} \in \mathbb{R}^n$ in DCNN, the cost function can accommodate n first derivatives and $\frac{n(n+1)}{2}$ second derivatives, which include unique cross derivatives.